

First-principles calculation of lattice thermal conductivities of α -, β -, and γ - Si_3N_4

Kazuyoshi Tatsumi,^{1,2,*} Atsushi Togo,² and Isao Tanaka^{2,3,4}

¹*Institute of Materials and Systems for Sustainability,
Nagoya University, Chikusa, Nagoya 464-8603, Japan*

²*Center for Elements Strategy Initiative for Structural Materials,
Kyoto University, Sakyo, Kyoto 606-8501, Japan*

³*Department of Materials Science and Engineering,
Kyoto University, Sakyo, Kyoto 606-8501, Japan*

⁴*Nanostructures Research Laboratory, Japan Fine Ceramics Center, Atsuta, Nagoya 456-8587, Japan*

The lattice thermal conductivities of α -, β - and γ - Si_3N_4 phases are investigated from first-principles anharmonic phonon calculations and linearized phonon Boltzmann transport equation. At 300 K, the lattice thermal conductivity of β - Si_3N_4 is calculated as $\kappa_{xx} = 73$ and $\kappa_{zz} = 199$ (in units of $\text{W m}^{-1} \text{K}^{-1}$), which is consistent with the reported experimental values of 69 and 180, respectively. For α - Si_3N_4 , $\kappa_{xx} = 68$ and $\kappa_{zz} = 100$ are obtained. The difference in anisotropy between these phases originates from the characteristic differences in their phonon band structures, which is closely related to the crystal structures. In α - Si_3N_4 , acoustic-mode phonons below 6 THz are the main heat carriers, while in β - Si_3N_4 , the phonon modes up to 12 THz contribute to the lattice thermal conductivity. For γ - Si_3N_4 , $\kappa = 77$ is obtained and its distribution of phonon mode contributions to the lattice thermal conductivity with respect to phonon frequency closely resembles that for κ_{xx} of β - Si_3N_4 , although the phonon lifetimes of γ - Si_3N_4 are half as short as those of β - Si_3N_4 .

I. INTRODUCTION

Several nitride insulators are known to exhibit high thermal conductivity, which is important for heat transfer materials at elevated temperatures. For example, Slack *et al.*¹ reported that wurtzite-type AlN has thermal conductivity that exceeds $100 \text{ W m}^{-1} \text{ K}^{-1}$. Si_3N_4 has become another promising thermal conductive insulator because its thermal conductivity has been improved up to $177 \text{ W m}^{-1} \text{ K}^{-1}$ through the use of advanced ceramic technologies related to densification and microstructure control.^{2–5} The Si_3N_4 ceramics also exhibit high mechanical strength at elevated temperatures; therefore, they are regarded as ideal materials for use in various applications, such as engine components, gas turbines, and heat sink substrates of power semiconductor devices.

At atmospheric pressure, Si_3N_4 has two phases, α and β , which are generally considered as low- and high-temperature phases, respectively.^{2,6,7} Their crystal structures belong to the $P31c$ and $P6_3/m$ space groups, respectively.^{8,9} These crystal structures are made of layers that stack along c -axis. Each layer is composed of SiN_4 tetrahedron units, which is equivalent between these two phases. However, their manners of the stackings are different.¹⁰ Fig. 1 depicts these layer structures from the principal axis direction. They are denoted as A, B, C, and D in the α phase, and A and B in the β phase. The stacking manners are thus ABCDABCD... and ABAB..., respectively. The α phase has additional two layer structures of C and D, which are related to A and B by the c glide operation.¹⁰ Along c -axis, the lattice constant of the α phase is approximately twice as long as that of the β phase.

The experimental thermal conductivities^{2–5,12} of the Si_3N_4 polymorphs were measured for bulk polycrystalline

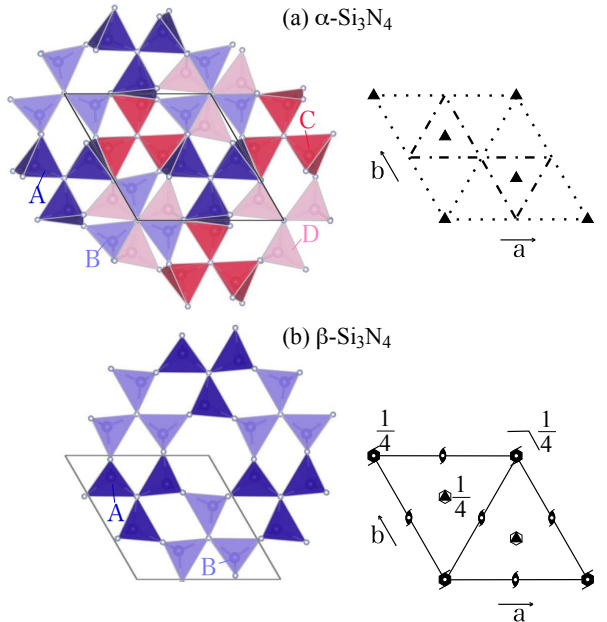


FIG. 1. (color online) Crystal structures of α - and β - Si_3N_4 . Stackings of SiN_4 tetrahedron layers are shown at the left. (a) ABCDABCD... for α - Si_3N_4 . (b) ABAB... for β - Si_3N_4 . Space group diagrams¹¹ for $P31c$ (α - Si_3N_4) and $P6_3/m$ (β - Si_3N_4) are shown on the right.

samples. These values were significantly affected by the lattice defects, impurities, shapes and orientations of the constituent crystal grains;⁶ the intrinsic thermal conductivity of defect-free Si_3N_4 has not been established. As an experimental approach to determine this, Li *et al.*¹³ applied the high-resolution thermoreflectance microscopy

to single $\beta\text{-Si}_3\text{N}_4$ grains in a ceramic sample and they obtained the lattice thermal conductivities of $\kappa_{xx} = 69$ and $\kappa_{zz} = 180 \text{ W m}^{-1} \text{ K}^{-1}$ at room temperature,¹⁴ showing large anisotropy of $\kappa_{zz}/\kappa_{xx} \sim 2.6$. For single-crystal grains of α and γ phases, thermal conductivity values by experiments are not known.

Hirosaki *et al.*⁶ theoretically estimated κ by application of the Green-Kubo formulation to the molecular dynamics (MD) method with the interatomic potentials proposed by Vashishta *et al.*¹⁵ They calculated κ_{xx} and κ_{zz} of $\beta\text{-Si}_3\text{N}_4$ to be 170 and $450 \text{ W m}^{-1} \text{ K}^{-1}$ at 300 K, respectively. Although the calculation showed much larger κ_{xx} and κ_{zz} than the experimental values by Li *et al.*, the ratio, $\kappa_{zz}/\kappa_{xx} \sim 2.6$, was well reproduced. For α -phase, they presented $\kappa_{xx} = 105$ and $\kappa_{zz} = 225$ at 300 K, for which the ratio $\kappa_{zz}/\kappa_{xx} \sim 2.1$ is smaller than that of α -phase. This indicates that the different stacking manners between the α and β may result in different anisotropy of lattice thermal conductivities.

Based on first principles anharmonic phonon calculations and linearized phonon Boltzmann transport equation¹⁶, Togo *et al.* recently calculated lattice thermal conductivities of compounds with 33 different chemical compositions that are known to have either zincblende- or wurtzite-type structures. These crystal structures are only different in their stacking manners of the densest atomic planes: ABCABC... for zincblende-type and ABAB... for wurtzite-type. Following this fact, in their calculations, lattice thermal conductivities of both zincblende- and wurtzite-type structures were calculated for each chemical composition and were compared. As a result, it was found that the different stacking manners differentiate little not only the lattice thermal conductivities, but the phonon lifetimes and the phonon densities of states (DOS).¹⁶ Therefore, making crystal structures have different stacking manners does not always bring the different lattice thermal conductivities.

In this study, we have investigated the lattice thermal conductivities of α and β phases of Si_3N_4 by using the first principles phonon calculations and linearized Boltzmann transport equation. This calculation has recently become possible to apply to crystalline phases of compounds systematically due to increase computer power and efforts on methodological and software developments. The calculated values are often more reliable than the other theoretical approach at this moment. In addition, using this approach, the microscopic analysis from the phonon picture is easily achieved, which is important in understanding the mechanism of thermal transport in crystals. By this, we achieved detailed analysis of lattice thermal conductivities of α and β phases and discussed about the different anisotropies of κ_{zz}/κ_{xx} between them.

In addition to the α and β phases, a cubic spinel phase ($\gamma\text{-Si}_3\text{N}_4$) is known to form upon compression and *in situ* heating.^{17,18} The reported transition pressures are scattered from 10 to 36 GPa, depending on the experimental

conditions.¹⁹ The γ phase is experimentally quenched to atmospheric pressure and room temperature. The thermal conductivity of the γ phase has not been experimentally reported, although it has been estimated by the Slack model (see Table IV).²⁰ For systematic understanding throughout the Si_3N_4 phases, we calculated lattice thermal conductivities of the γ phase.

The present study aims to qualitatively elucidate the lattice thermal conductivity tensors among the three Si_3N_4 phases. After the methodology is described, we examine the validity of the present results through comparison of the calculated thermal properties with the available experimental and theoretical references. The characteristic behaviors of the lattice thermal conductivities are then investigated in details.

II. COMPUTATIONAL PROCEDURES

A. Lattice thermal conductivity calculation

The lattice thermal conductivities were calculated by solving the linearized Boltzmann transport equation (LBTE)²¹ within the single-mode relaxation time approximation (RTA)²². The harmonic phonons and lattice thermal conductivities were calculated with the phonopy²³ and phono3py¹⁶ software packages. Lattice thermal conductivity calculated with the single-mode RTA often underestimate the full solution of LBTE.^{16,24,25} For diamond, this difference is significant, but not for silicon and germanium.²⁶ We calculated lattice thermal conductivities of the three Si_3N_4 phases at 300 K without isotope effect by using the direct solution of LBTE²⁷, which is one of LBTE full solutions, and compared with those by the single mode RTA as shown in Table I. Except for κ_{zz} of the β phase, the differences were found trivial. κ_{zz} of the β phase was 13 % larger in the direct solution. Though this difference is not negligible, we consider that the impact to our qualitative discussion in the following sections is minor. It is rather important to employ the single mode RTA solution for the simple analysis in the closed form of the lattice thermal conductivity (Eq. (5)) by independent phonon modes as the heat carriers.

TABLE I. Comparison of latteice thermal conductivies ($\text{W K}^{-1} \text{ m}^{-1}$) at 300 K calculated by the single-mode RTA and by the direct solution of LBTE without considering isotope effect.

	$\alpha\text{-Si}_3\text{N}_4$		$\beta\text{-Si}_3\text{N}_4$		$\gamma\text{-Si}_3\text{N}_4$
	κ_{xx}	κ_{zz}	κ_{xx}	κ_{zz}	κ
Single-mode RTA	70	102	76	210	82
Direct solution	69	102	76	238	82

In the following sections, we denote the phonon mode by $\lambda \equiv (\mathbf{q}, p)$ with the set of the phonon wave vector

\mathbf{q} and band index p and $-\lambda \equiv (-\mathbf{q}, p)$. The harmonic phonon frequency of the phonon mode λ is denoted by ω_λ . The single-mode relaxation time for the lattice thermal conductivity by the phonon-phonon interaction is approximated by the phonon lifetime given as

$$\tau_{\lambda, \text{ph-ph}} = \frac{1}{2\Gamma_\lambda(\omega_\lambda)}$$

with

$$\Gamma_\lambda(\omega) = \frac{18\pi}{\hbar^2} \sum_{\lambda' \lambda''} |\Phi_{-\lambda \lambda' \lambda''}|^2 N_2(\mathbf{q}, \omega), \quad (1)$$

where \hbar is the reduced Planck constant. $\Phi_{\lambda \lambda' \lambda''}$ denotes the three-phonon-scattering strength obtained by the usual coordinate transformation of third-order force constants from direct space to phonon space.¹⁶ The second- and third-order real-space force constants were obtained by first-principles calculations, for which the details are given in Sec. II B. $N_2(\mathbf{q}, \omega)$ is the weighted joint DOS (WJDOS)¹⁶,

$$N_2(\mathbf{q}, \omega) = N_2^{(1)}(\mathbf{q}, \omega) + N_2^{(2)}(\mathbf{q}, \omega) \quad (2)$$

with

$$N_2^{(1)} = \frac{1}{N_{\mathbf{q}}} \sum_{\lambda' \lambda''} (n_{\lambda'} - n_{\lambda''}) \Delta(-\mathbf{q} + \mathbf{q}' + \mathbf{q}'') \\ \times [\delta(\omega + \omega_{\lambda'} - \omega_{\lambda''}) - \delta(\omega - \omega_{\lambda'} + \omega_{\lambda''})], \quad (3)$$

$$N_2^{(2)} = \frac{1}{N_{\mathbf{q}}} \sum_{\lambda' \lambda''} (n_{\lambda'} + n_{\lambda''} + 1) \Delta(-\mathbf{q} + \mathbf{q}' + \mathbf{q}'') \\ \times \delta(\omega - \omega_{\lambda'} - \omega_{\lambda''}), \quad (4)$$

where $\Delta(\mathbf{q} + \mathbf{q}' + \mathbf{q}'')$ being 1 if $\mathbf{q} + \mathbf{q}' + \mathbf{q}''$ equals to a reciprocal lattice vector, and otherwise zero. This constraint comes from the lattice translational invariance of force constants and is included in $\Phi_{\lambda \lambda' \lambda''}$ ¹⁶. However, we let it appear redundantly in Eqs. (3) and (4) for using in Sec. III. $N_{\mathbf{q}}$ is the number of \mathbf{q} -points. $n_\lambda = [\exp(\hbar\omega_\lambda/k_B T) - 1]^{-1}$ is the Bose-Einstein distribution at temperature T where k_B is the Boltzmann constant.

Lattice thermal conductivity κ within the single-mode RTA is written in the closed form:

$$\kappa = \frac{1}{N_{\mathbf{q}} \Omega} \sum_{\lambda} \tau_{\lambda} \mathbf{v}_{\lambda} \otimes \mathbf{v}_{\lambda} c_{\lambda}, \quad (5)$$

where Ω is the unit cell volume, $\mathbf{v}_{\lambda} = \nabla_{\mathbf{q}} \omega_{\lambda}$ is the group velocity and $c_{\lambda} = \frac{\partial(n_{\lambda} \hbar \omega_{\lambda})}{\partial T}$ is the mode heat capacity. To analyze the lattice thermal conductivity in detail, we define cumulative thermal conductivity $\kappa^c(\omega)$ as

$$\kappa^c(\omega) = \frac{1}{N_{\mathbf{q}} \Omega} \int_0^{\omega} \sum_{\lambda} \tau_{\lambda} \mathbf{v}_{\lambda} \otimes \mathbf{v}_{\lambda} c_{\lambda} \delta(\omega' - \omega_{\lambda}) d\omega', \quad (6)$$

and its derivative:

$$\frac{d\kappa^c(\omega)}{d\omega} = \frac{1}{N_{\mathbf{q}} \Omega} \sum_{\lambda} \tau_{\lambda} \mathbf{v}_{\lambda} \otimes \mathbf{v}_{\lambda} c_{\lambda} \delta(\omega - \omega_{\lambda}) \quad (7)$$

to draw the distribution of phonon mode contributions to the lattice thermal conductivity.

B. Computational details

To compare the calculated lattice thermal conductivities with the measured values, the isotopic scattering effect with the natural isotope distribution was taken into account according to the second-order perturbation theory.²⁸ Using the single mode relaxation time by phonon-phonon scattering $\tau_{\lambda, \text{ph-ph}}$ and by isotopic scattering $\tau_{\lambda, \text{iso}}$, the total single mode relaxation time τ_{λ} was approximated by assuming Matthiessen's rule, $1/\tau_{\lambda} = 1/\tau_{\lambda, \text{ph-ph}} + 1/\tau_{\lambda, \text{iso}}$.

The force constants were calculated using the projector augmented wave method²⁹ within the framework of density functional theory as implemented in the VASP code.^{30–32} The generalized gradient approximation (GGA) parameterized by Perdew, Burke, and Ernzerhof³³ was used for the exchange correlation potential. A plane wave energy cutoff of 500 eV was employed. Crystal structures were optimized at 0 GPa until the residual forces acting on the constituent atoms were less than 10^{-6} eV Å⁻¹ by the first-principles calculations, i.e., equilibrium volume change due to zero point energy of phonons was not considered.

The calculated and experimental lattice parameters are shown in Table II. The present results are in agreement with the experimental data within +0.7 % error. The lattice volume optimized with the local density approximation (LDA) according to Ceperley and Alder as parameterized by Perdew and Zunger^{34,35} for β -Si₃N₄ was 3 % smaller than the volume optimized with GGA, which is a typical volume contraction of LDA. κ_{xx} and κ_{zz} calculated with LDA were larger by 0.3 and 2.6 % than those calculated with GGA using the respective calculated lattice parameters. For our discussion, these differences are sufficiently small; therefore, the impact of the choice of exchange correlation potential is considered to be minor in this study.

TABLE II. Lattice parameters of three Si₃N₄ phases by calculations (this work) and experiments in Å.

	α -Si ₃ N ₄		β -Si ₃ N ₄		γ -Si ₃ N ₄
	a	c	a	c	a
Exp.	7.7545 ^a	5.62145 ^a	7.6044 ^b	2.9063 ^b	7.7351 ^c
Calc.	7.81	5.66	7.66	2.93	7.79

^a Yashima *et al.*⁸.

^b Du Boulay *et al.*⁹.

^c Paszkowicz *et al.*³⁶.

The force constants were calculated by the finite displacement approach³⁷ with 0.03 Å displacement distance. For this calculation, the following supercells were adopted: 1 × 1 × 2, 1 × 1 × 3, and 1 × 1 × 1 supercells of the conventional unit cells for the calculations of the third-order force constants of α , β , and γ -Si₃N₄, respectively, and 3 × 3 × 4, 3 × 3 × 8 and 2 × 2 × 2 for those of the second-order force constants. Table III shows lattice

TABLE III. Calculated lattice thermal conductivities (LTC) of α -, β -, and γ - Si_3N_4 ($\text{W K}^{-1} \text{m}^{-1}$) at 300 K with respect to several combinations of supercell sizes. The lattice thermal conductivities are shown without and with (in parenthesis) considering isotope effect. The values in parenthesis for the supercell sizes are the numbers of atoms in the supercells.

Phase	Supercell (number of atoms)		LTC	
	Third order	Second order	xx	zz
α	$1 \times 1 \times 1$ (28)	$1 \times 1 \times 1$ (28)	37(37)	58(57)
	$1 \times 1 \times 2$ (56)	$1 \times 1 \times 2$ (56)	42(41)	81(79)
	$1 \times 1 \times 1$ (28)	$2 \times 2 \times 2$ (224)	56(55)	84(81)
	$1 \times 1 \times 2$ (56)	$2 \times 2 \times 2$ (224)	69(67)	98(95)
	$1 \times 1 \times 2$ (56)	$2 \times 2 \times 3$ (336)	69(68)	101(97)
β	$1 \times 1 \times 2$ (56)	$3 \times 3 \times 4$ (1008)	70(68)	103(100)
	$1 \times 1 \times 2$ (28)	$1 \times 1 \times 2$ (28)	45(44)	178(173)
	$1 \times 1 \times 2$ (28)	$2 \times 2 \times 4$ (224)	79(76)	219(208)
	$1 \times 1 \times 3$ (42)	$2 \times 2 \times 4$ (224)	74(71)	205(194)
	$1 \times 1 \times 3$ (42)	$2 \times 2 \times 5$ (280)	75(72)	207(196)
γ	$1 \times 1 \times 3$ (42)	$3 \times 3 \times 8$ (1008)	76(73)	210(199)
	$1 \times 1 \times 1$ (56)	$1 \times 1 \times 1$ (56)	76(72)	
	$1 \times 1 \times 1$ (56)	$2 \times 2 \times 2$ (448)	82(77)	
γ	$1 \times 1 \times 1$ (56)	$3 \times 3 \times 3$ (1512)	83(79)	

thermal conductivities calculated with several different sets of the supercell sizes. Increasing the supercell sizes, we can see the lattice thermal conductivities are converging. Therefore our choices of supercell sizes are considered reasonable. We assumed that γ phase is quenchable to 0 GPa from the high pressure where the γ phase can form. We calculated the lattice thermal conductivity of the γ phase at 0, 10, 20, and 40 GPa and observed that they are smoothly connected by a straight line as shown in Fig. 2. Obviously no imaginary modes were found at these pressures. Therefore, we consider that the phonon properties of the γ phase are reasonably compared with the α and β phases at 0 GPa.

Uniform \mathbf{k} -point sampling meshes of $4 \times 4 \times 2$, $4 \times 4 \times 3$, and $3 \times 3 \times 3$ were employed for the calculations of the third-order force constants of the α , β , and γ phases, respectively. For the α and β phases, the centers of the a^*b^* planes in the reciprocal cell were sampled, while the centers on the c^* -axes were not. For the γ phase, a non- Γ center mesh was used. For the calculations of the second-order force constants, the Γ -points of the α and β phases were only sampled, and the only one \mathbf{k} -point at $(0.5, 0.5, 0.5)$ was sampled for the γ phase. The \mathbf{q} -point sampling meshes of $10 \times 10 \times 14$, $10 \times 10 \times 26$, and $18 \times 18 \times 18$ were employed in the calculations of Eq. (5) for the α , β , and γ phases, respectively.

Non-analytical term correction was applied to the second-order force constants to take into account the long range dipole-dipole interaction.³⁸ For this correction, static dielectric constants and Born effective charges were calculated using the density functional perturbation

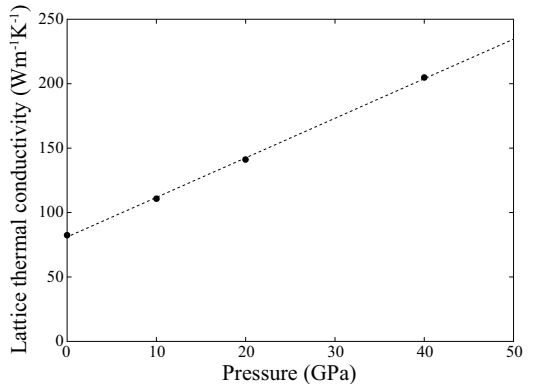


FIG. 2. (color online) Lattice thermal conductivity of γ - Si_3N_4 at 300 K as a function of pressure without considering isotope effect. The dotted line is obtained by the least square fitting to the points.

theory as implemented in the VASP code^{39,40}.

III. RESULTS AND DISCUSSION

A. Lattice thermal conductivities

TABLE IV. Calculated lattice thermal conductivities ($\text{W m}^{-1} \text{K}^{-1}$) of α - Si_3N_4 , β - Si_3N_4 , and γ - Si_3N_4 without and with (in parenthesis) considering isotope effect at 300 K compared with the experimental and theoretical reference data.

	α - Si_3N_4		β - Si_3N_4		γ - Si_3N_4
	κ_{xx}	κ_{zz}	κ_{xx}	κ_{zz}	κ
This work	70(68)	103(100)	76(73)	210(199)	82(77)
Calc. ^a	105	225	170	450	-
Calc. ^b		70		250	80
Exp. ^c	-	-	69	108	-

^a Hirosaki *et al.*⁶, molecular dynamics simulation (Green-Kubo).

^b Morelli and Heremans,²⁰ Slack model.

^c Li *et al.*¹³, single crystalline grains of poly-crystals.

Table IV shows the calculated κ for 300 K with the isotope effect. β - Si_3N_4 has a markedly more anisotropic κ than α - Si_3N_4 . The directional averages $\sum_i \kappa_{ii}/3$ are 79, 115, and 77 $\text{W m}^{-1} \text{K}^{-1}$ for the α , β , and γ phases, respectively. The value for the γ phase is similar to that for the α phase, despite the comparatively large difference among the bulk moduli (B) that are also shown in Table IV.

Table IV also lists the previously reported experimental¹³ and theoretical⁶ κ for reference. The theoretical results²⁰ of the Slack model, which do not include the anisotropy in κ , are shown as κ in Table IV. Compared to the κ from MD⁶, our κ for the β phase has better agreement with the experimental κ . Compared to

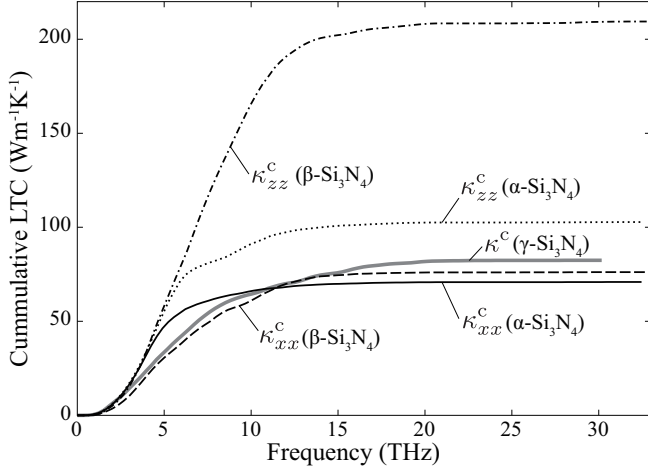


FIG. 3. Cumulative lattice thermal conductivity (LTC) ($\text{W m}^{-1} \text{K}^{-1}$) of the three Si_3N_4 phases without considering isotope effect at 300 K. Solid and dotted curves show κ_{xx}^c and κ_{zz}^c of $\alpha\text{-Si}_3\text{N}_4$, respectively. Dashed and dashed-dotted curves give κ_{xx}^c and κ_{zz}^c of $\beta\text{-Si}_3\text{N}_4$, respectively, and gray solid curve depicts κ^c of $\gamma\text{-Si}_3\text{N}_4$.

κ from the Slack model, our directional average $\sum_i \kappa_{ii}/3$ is also much closer to the experimental average.

Fig. 3 shows the cumulative thermal conductivity, $\kappa^c(\omega)$, with the isotope effect. From this figure, it is evident that in the α , β , and γ phases, the phonon modes with their frequencies up to ~ 6 , 12 and 10 THz largely contribute to each respective κ . Thus we investigate the phonon modes in these frequency ranges.

B. Distribution of group velocity in Brillouin zone

The Brillouin zones and phonon band diagrams of the three phases are shown in Fig. 4 (a). In this figure, we investigate the gradient of ω_λ , the group velocity projected on the paths along the nonequivalent axes of the reciprocal lattice. We particularly focus on the anisotropy of the group velocity in the α and β phases. This was not investigated in the previous works^{19,41}. The band diagrams on the other high-symmetry paths are almost identical to those reported^{19,41} and thus are not shown. For the α and β phases, in order to investigate the distribution of the group velocities all over the Brillouin zone, the cross-sections of the phonon frequency distributions for the band indices $p=1, 2, 3$ and 4 are shown in Fig. 4 (b). As seen in Fig. 3, the frequencies for these band indices cover a large part of the frequency ranges where κ^c increase significantly. The cross-sections are on the b^*c^* plane. There were negligible differences among the cross-sections on the planes containing c^* axis, we focus on the b^*c^* plane as a representative of all such planes. The $A-\Gamma$ and $\Gamma-K$ paths of the band diagram respectively correspond to the left and bottom end lines in the cross-section area. Thus, the distribution profiles

on the end lines appear in the dispersion curves in the band diagrams. Just for clarification purposes, the dispersion curves corresponding to the profiles for $p=4$ are highlighted by gray color.

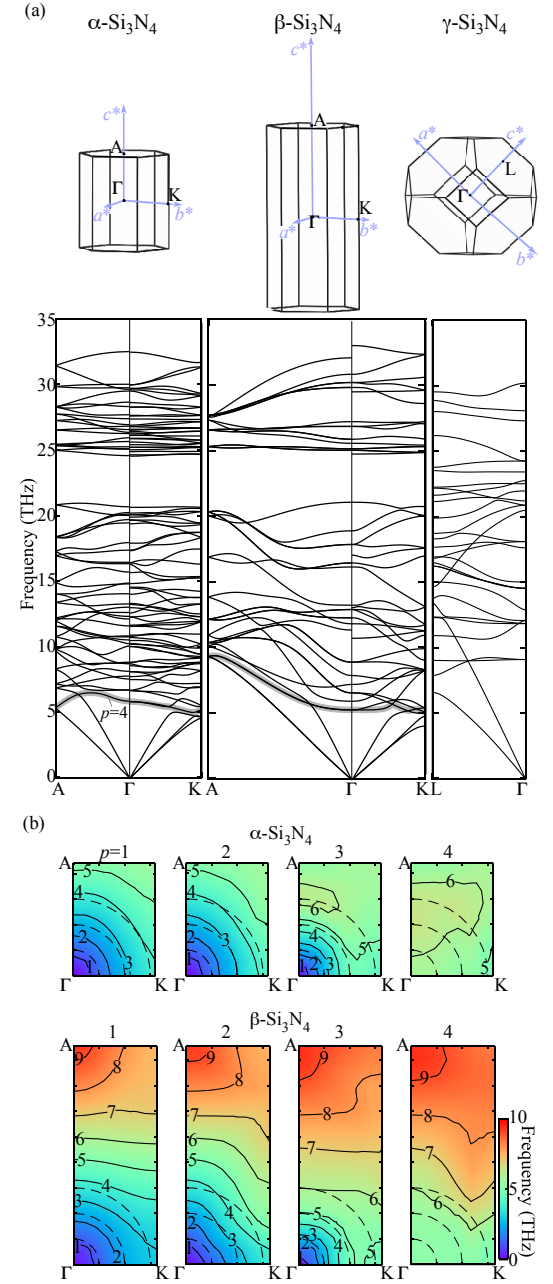


FIG. 4. (color online) (a) Brillouin-zones and band diagrams of the three phases. (b) Contour maps of phonon frequencies for the α and β phases, on the b^*c^* planes of Brillouin-zones. The maps for the four lowest-frequency phonon modes ($p=1, 2, 3$, and 4) are shown. In the band diagrams for the α and β phases, the dispersion curve for $p=4$ is denoted by a thick gray line.

In the band diagram of the α phase, the dispersion relation on the $A-\Gamma$ path for a band index is similar to

that on the K- Γ path. This suggests nearly isotropic group velocities, which is more clearly seen in the cross-sections for $p=1, 2$ and 3 , where the most of the contour lines are nearly parallel to the circular dash lines inserted as a guide. In contrast, in the band diagram of the β phase, the dispersion relation is much more different between the two paths. For example, the frequencies of the acoustic-mode phonons at the A point are much higher than those at the K point. Consistently, the gradients of frequencies in the cross-sections are, in the most part, parallel to the vertical edges; the group velocities orient closely to the c^* axis direction. This difference in group velocities between the α and β phases is due to the A- Γ path lengths. The β phase has an approximately twice longer path than the α phase; the lattice constant c of the β phase is nearly half that of the α phase, owing to the different stacking manners of the basal layer structures (Fig. 1). Comparing the cross-sections for $p=4$ between the α and β phases, the β phase has larger gradients of frequencies than the α phase. Comparing the band diagrams of the α and β phases, the same tendency is also seen for the most of the other optical phonon modes.

In the γ phase, the dispersion curve for the longitudinal acoustic mode-phonons is almost linear. Their frequencies at the L point is much higher than the longitudinal acoustic phonon frequencies at the A or K points of the α and β phases. The gradients of the acoustic phonon branches near the Γ point are the largest among the three phases, as expected by the largest B .

C. Microscopic analysis on κ behavior

In the previous section, we have investigated the anisotropy in \mathbf{v}_λ , which may explain the anisotropy in $\boldsymbol{\kappa}$. Here we examine which terms in Eq.(5) characterize the behavior of the calculated $\boldsymbol{\kappa}$. In the following, we omit the term of mode heat capacity because it is approximately constant for the phonon modes that mainly carry heat at 300 K. For simplicity, the effect of isotope scattering is not considered in this section. For the investigation, the derivative of cumulative thermal conductivity, $d\boldsymbol{\kappa}^c/d\omega$ in Eq.(7), is shown at the top of Fig. 5.

Assuming that τ_λ and \mathbf{v}_λ are constant, then $d\boldsymbol{\kappa}_{ii}^c/d\omega$ ($ii=xx, zz$) are proportional to the phonon DOS:

$$g(\omega) = \frac{1}{N_{\mathbf{q}}} \sum_{\lambda} \delta(\omega - \omega_{\lambda}). \quad (8)$$

We refer to $g(\omega)/\Omega$ as a frequency distribution of a heat carrier density. Alternatively, assuming that only τ_λ is constant, then $d\boldsymbol{\kappa}^c/d\omega$ is proportional to:

$$\mathbf{h}(\omega) = \frac{1}{N_{\mathbf{q}}\Omega} \sum_{\lambda} \mathbf{v}_\lambda \otimes \mathbf{v}_\lambda \delta(\omega - \omega_{\lambda}), \quad (9)$$

from which we examine the impacts of both of \mathbf{v}_λ and the heat carrier density. $g(\omega)/\Omega$ and $\mathbf{h}(\omega)$ are shown

in Figs. 5 (b) and (c). As for the frequency variation of $\tau_{\lambda,\text{ph-ph}}$, scatter plots of $(\tau_{\lambda,\text{ph-ph}}, \omega_{\lambda})$ are shown in Fig. 5 (d).

Comparison of the α and β phases indicates their phonon lifetimes distributions are qualitatively similar, except for a striking difference below ~ 5 THz, which will be examined later. The markedly different $d\boldsymbol{\kappa}_{ii}^c/d\omega$ between the two phases are therefore ascribed to the corresponding h_{ii} . The overall spectral shapes of $g(\omega)/\Omega$ are also similar between the two phases; therefore, \mathbf{v}_λ alone accounts for the different behavior of $d\boldsymbol{\kappa}_{ii}^c/d\omega$. It is thus concluded that the different anisotropy in $\boldsymbol{\kappa}$ can be qualitatively explained by the different \mathbf{v}_λ . In contrast, for the zincblende and wurtzite structures, the group velocities of these structures are suggested to be similar from their band structures¹⁶. This must result in similar $\boldsymbol{\kappa}$ between these structures, irrespective of the stacking manner.

The γ phase has much different $g(\omega)/\Omega$, $\mathbf{h}(\omega)$, and $\tau_{\lambda,\text{ph-ph}}$ from the other phases, as expected from the large differences in their crystal structures. The most significant difference is in the phonon lifetimes. For 4 THz $\lesssim \omega_{\lambda} \lesssim 10$ THz, the phonon lifetimes are approximately half as short as those of the other phases. We will examine this in detail later. As a result, $d\boldsymbol{\kappa}_{xx}^c/d\omega$ has relatively low intensities. The longitudinal acoustic phonon branch increases its frequencies much significantly, as we have examined in the band diagram; therefore, $d\boldsymbol{\kappa}_{xx}^c/d\omega$ rather gradually attenuates as the frequency increases, occasionally resembling $d\boldsymbol{\kappa}_{xx}^c/d\omega$ of the β phase.

D. Phonon properties characterizing $\tau_{\lambda,\text{ph-ph}}$

The distribution of phonon lifetimes is qualitatively similar between the α and β phases, although their group velocities have marked differences. This remains a curiosity. Recalling Eq. (1), $\tau_{\lambda,\text{ph-ph}}$ in the present form is dependent on WJDOS and $|\Phi_{\lambda\lambda'\lambda''}|^2$. We examine these terms one-by-one.

The frequency profiles of WJDOS in Fig. 6 are very similar between the α and β phases, for each different \mathbf{q} -points. Their intensities are scaled with Z^2 of which Z is the number of formula units in the primitive unit cell, to compare WJDOS for structures with different Z . These profiles show weak \mathbf{q} -point dependences. The frequency profile for the γ phase is only shown at $\mathbf{q} = (0, 0, 0)$ because of the different shape of the Brillouin zone from those in the other phases. We checked that the \mathbf{q} dependence of WJDOS for the γ phase was as weak as those shown in Fig. 6 for the α and β phases. The intensities of WJDOS below ~ 10 THz in the γ phase are slightly smaller than those in the other phases.

As for $|\Phi_{\lambda\lambda'\lambda''}|^2$, in Table. V, they are averaged over two frequency ranges of 0–15 or 0–35 THz for ω_{λ} and all indices in λ' and λ'' . The frequency ranges for ω_{λ} were set so that the narrower frequency range approximately corresponds to the range where the phonon modes largely contribute to $\boldsymbol{\kappa}$. A small change in the frequency range

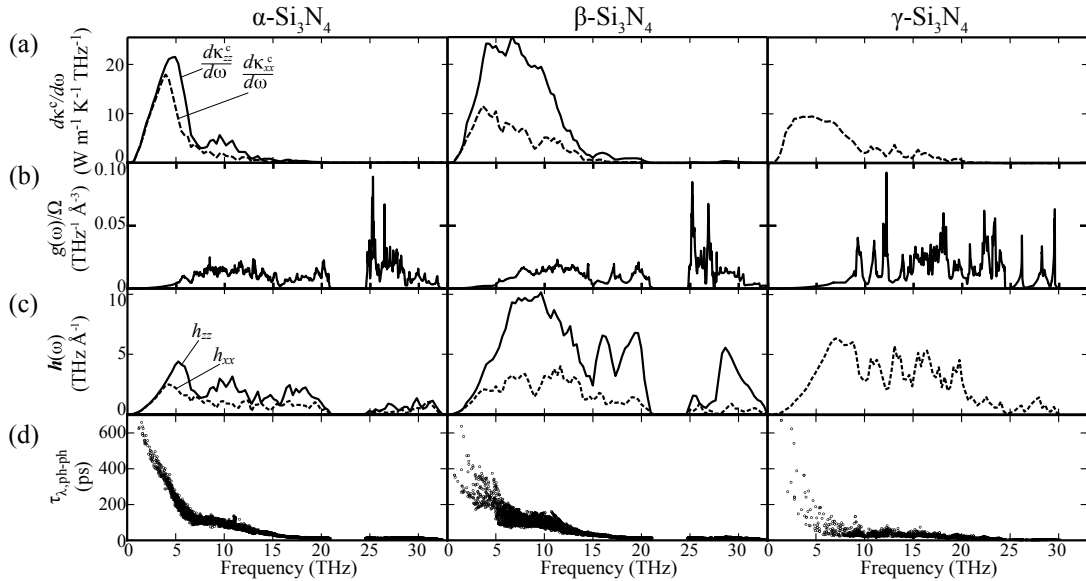


FIG. 5. Microscopic phonon properties of three Si_3N_4 phases. (a) Cumulative thermal conductivity κ^c and its frequency derivative, (b) DOS as $g(\omega)$, (c) DOS weighted with $\mathbf{v}_\lambda \otimes \mathbf{v}_\lambda$ as $h(\omega)$, and (d) scatter plots of phonon lifetimes and phonon frequencies, ($\tau_\lambda, \omega_\lambda$).

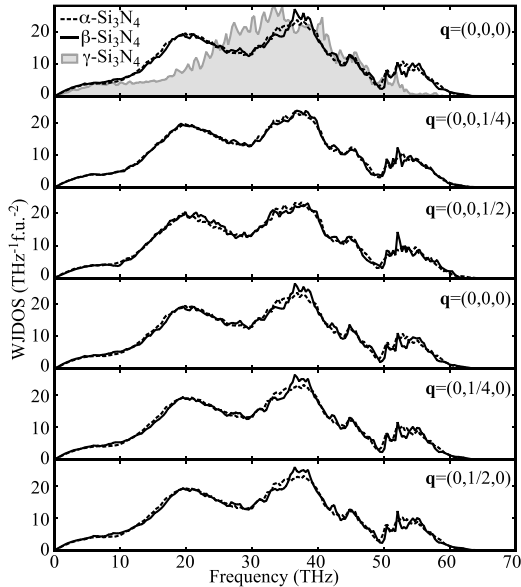


FIG. 6. WJDOS of α - and β - Si_3N_4 at different \mathbf{q} points and that of γ - Si_3N_4 at the Γ point. The WJDOS for the α and β phases in the first and fourth rows are calculated at the same Γ -point but with the polarization for the non-analytic term correction set along c^* and b^* , respectively.

by a few terahertz did not change the qualitative characteristics of the averages. To compare the averages among the phases having different Z , as in Ref. 42 we multiply the average by $(3n_a)^2$ where n_a is the number of atoms in the primitive unit cell. The averages are very similar for

TABLE V. Averages of $|\Phi_{\lambda\lambda'\lambda''}|^2$ over frequency ranges of ω_λ (0–15 and 0–35 THz) and all (λ', λ'') . The values are in units of meV².

Frequency range (THz)	Phase		
	α	β	γ
0–15	0.47	0.46	1.02
0–35	2.30	2.30	2.02

the α and β phases. With the similar impact of the WJDOS and $|\Phi_{\lambda\lambda'\lambda''}|^2$, the phonon lifetimes in these phases are also similar. For the γ phase, the short τ_λ are attributed to the large $|\Phi_{\lambda\lambda'\lambda''}|^2$ in the narrower frequency range for ω_λ .

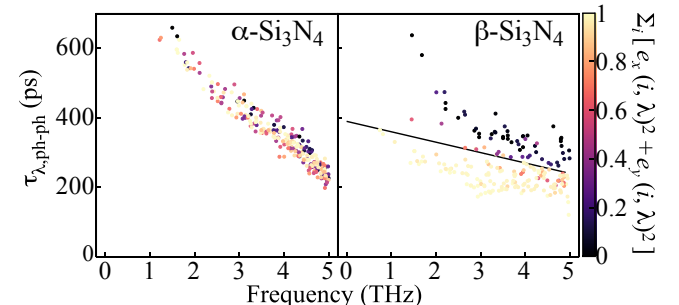


FIG. 7. (color online) Distribution of phonon lifetimes for $\omega_\lambda \leq 5$ THz shown in color with respect to the fraction of the eigenvector component (a) along \mathbf{q} and (b) parallel to the ab plane (b).

Finally, we examine the striking difference in Fig. 5 (d) below ~ 5 THz between the α and β phases. Fig. 7 enlarges that part. In the α phase, $\tau_{\lambda,\text{ph-ph}}$ below ~ 5 THz are distributed around a single smooth line, while for the β phase, they are scattered much more largely. In this figure, each plot is shown with a color specified by $\sum_i [e_x(i, \lambda)^2 + e_y(i, \lambda)^2]$, the fraction of the eigenvector component parallel to the ab plane.

From Fig. 7, we find that, for the β phase, a phonon mode of the atomic vibration parallel to the ab plane is more hindered by the other phonons than a phonon mode of the vibration perpendicular to the plane. A straight line is inserted in the graph for β phase in Fig. 7. The numbers of the phonon modes below and above the line are 145 and 67, whose ratio is reasonable as the population ratio between the two groups of the phonon modes whose atomic vibrations are, respectively, parallel and perpendicular to the ab plane.

IV. SUMMARY

In the present study, the lattice thermal conductivities of the three Si_3N_4 phases were investigated using lattice dynamics based on the first-principles interatomic force constants. The main remarks are as follows:

- 1) In α - and β - Si_3N_4 , of which the crystal structures

are characterized by the stacking manner of the basal layer structures, κ is largely altered due to the differences in the harmonic band structures induced by the different stacking manners. This is in contrast with the zincblende and wurtzite structures in the previous study¹⁶. κ for α - Si_3N_4 is rather isotropic, while κ_{zz} for the β phase is twice or more larger than the other κ_{ii} of the three phases.

2) In the α phase, the acoustic-mode phonons below 6 THz are the main heat carriers, while in the β phase, the phonons below 12 THz contribute to κ . Their group velocities are confirmed to characterize the behavior of κ .

3) In the γ phase, the frequency distribution of the phonon mode contributions to κ is similar to that for κ_{xx} of β - Si_3N_4 , which is attributed to its large phonon-phonon scattering strength and steep longitudinal acoustic branches.

ACKNOWLEDGMENTS

The present work was partly supported by a Grant-in-Aid for Scientific Research (No. 15K14108 from the Ministry of Education, Culture, Sports, Science and Technology (MEXT) Japan and the Elements Strategy Initiative for Structural Materials (ESISIM) of Kyoto University.

* k-tatsumi@imass.nagoya-u.ac.jp

- ¹ G. Slack, Journal of Physics and Chemistry of Solids **34**, 321 (1973).
- ² Y. Zhou, H. Hyuga, D. Kusano, Y.-i. Yoshizawa, and K. Hirao, Advanced Materials **23**, 4563 (2011).
- ³ K. Hirao, K. Watari, H. Hayashi, and M. Kitayama, MRS Bulletin **26**, 451 (2001).
- ⁴ K. Watari, Journal of the Ceramic Society of Japan **109**, S7 (2001).
- ⁵ N. Hirosaki, Y. Okamoto, M. Ando, F. Munakata, and Y. Akimune, Journal of the Ceramic Society of Japan **104**, 49 (1996).
- ⁶ N. Hirosaki, S. Ogata, C. Kocer, H. Kitagawa, and Y. Nakamura, Physical Review B **65**, 134110 (2002).
- ⁷ F. L. Riley, Journal of the American Ceramic Society **83**, 245 (2000).
- ⁸ M. Yashima, Y. Ando, and Y. Tabira, The Journal of Physical Chemistry B **111**, 3609 (2007).
- ⁹ D. Du Boulay, N. Ishizawa, T. Atake, V. Streltsov, K. Furuya, and F. Munakata, Acta Crystallographica Section B: Structural Science **60**, 388 (2004).
- ¹⁰ S. Hampshire, H. Park, D. Thompson, and K. Jack, Nature **274**, 880 (1978).
- ¹¹ T. Hahn, ed., International tables for crystallography, Vol. A (John Wiley & Sons, Inc., 2011).
- ¹² T. Hirai, S. Hayashi, and K. Niihara, AM. CERAM. SOC. BULL. Am. Ceram. Soc. Bull. **57**, 1126 (1978).
- ¹³ B. Li, L. Pottier, J. Roger, D. Fournier, K. Watari, and K. Hirao, Journal of the European Ceramic Society **19**, 1631 (1999).
- ¹⁴ K. Watari, Y. Seki, and K. Ishizaki, J. Ceram. Soc. Japan **97**, 174 (1989).
- ¹⁵ R. Vashishta, R. K. Kalia, A. Nakano, and I. Ebbsö, Amorphous Insulators and Semiconductors, edited by M. F. Thorpe and M. I. Mitkova (Kluwer, 1996).
- ¹⁶ A. Togo, L. Chaput, and I. Tanaka, Physical Review B **91**, 094306 (2015).
- ¹⁷ A. Zerr, G. Miehe, G. Serghiou, M. Schwarz, E. Kroke, R. Riedel, H. Fueß, P. Kroll, and R. Boehler, Nature **400**, 340 (1999).
- ¹⁸ Y. Zhang, A. Navrotsky, and T. Sekine, Journal of materials research **21**, 41 (2006).
- ¹⁹ B. Xu, J. Dong, P. F. McMillan, O. Shebanova, and A. Salamat, Physical Review B **84**, 014113 (2011).
- ²⁰ D. Morelli and J. Heremans, Applied Physics Letters **81**, 5126 (2002).
- ²¹ R. Peierls, Ann. Phys. **395**, 1055 (1929).
- ²² G. P. Srivastava, Physics of phonons (CRC Press, 1990).
- ²³ A. Togo and I. Tanaka, Scripta Materialia **108**, 1 (2015).
- ²⁴ S. Mukhopadhyay, L. Lindsay, and D. J. Singh, Scientific reports **6** (2016).
- ²⁵ A. Ward and D. Broido, Physical Review B **81**, 085205 (2010).
- ²⁶ A. Ward, D. A. Broido, D. A. Stewart, and G. Deinzer, Phys. Rev. B **80**, 125203 (2009).
- ²⁷ L. Chaput, Physical review letters **110**, 265506 (2013).
- ²⁸ S.-i. Tamura, Physical Review B **27**, 858 (1983).
- ²⁹ P. E. Blöchl, Phys. Rev. B **50**, 17953 (1994).
- ³⁰ G. Kresse and J. Furthmüller, Physical Review B **54**, 11169 (1996).

- ³¹ G. Kresse, J. Non-Cryst. Solids **193**, 222 (1995).
- ³² D. J. Kresse, Georg, Phys. Rev. B **59**, 1758 (1999).
- ³³ J. P. Perdew, K. Burke, and M. Ernzerhof, Phys. Rev. Lett. **77**, 3865 (1996).
- ³⁴ D. M. Ceperley and B. Alder, Physical Review Letters **45**, 566 (1980).
- ³⁵ J. P. Perdew and A. Zunger, Phys. Rev. B **23**, 5048 (1981).
- ³⁶ W. Paszkowicz, R. Minikayev, P. Piszora, M. Knapp, C. Bähitz, J. Recio, M. Marques, P. Mori-Sánchez, L. Gerward, and J. Jiang, Phys. Rev. B **69**, 052103 (2004).
- ³⁷ L. Chaput, A. Togo, I. Tanaka, and G. Hug, Phys. Rev. B **84**, 094302 (2011).
- ³⁸ Y. Wang, J. Wang, W. Wang, Z. Mei, S. Shang, L. Chen, and Z. Liu, J. Phys.: Condens. Matter **22**, 202201 (2010).
- ³⁹ M. Gajdoš, G. Hummer, G. Kresse, J. Furthmüller, and B. F, Phys. Rev. B **73**, 045112 (2006).
- ⁴⁰ S. Baroni and R. Resta, Phys. Rev. B **33**, 7017 (1986).
- ⁴¹ A. Kuwabara, K. Matsunaga, and I. Tanaka, Physical Review B **78**, 064104 (2008).
- ⁴² K. Mizokami, A. Togo, and I. Tanaka, Phys. Rev. B **97**, 224306 (2018).